Hierarchical MoS2/C@MXene composite as an anode for high-performance lithium-ion capacitors

Hierarchical MoS_2/C@MXene composite as an anode for high-performance lithium-ion capacitors

Yifan Jin[a], Shutian Tan[a], Zhengju Zhu[a], Ying He[a,b,*], Le Quoc Bao[c], Petr Saha[b], Qilin Cheng [a,b,*]

[a]*Key Laboratory for Ultrafine Materials of Ministry of Education, Shanghai Engineering Research Center of Hierarchical Nanomaterials, School of Materials Science and Engineering, East China University of Science and Technology, 200237 Shanghai, China*

[b]*Sino-EU Joint Laboratory of New Energy Materials and Devices, Tomas Bata University in Zlin, nam. T. G. Masaryka 5555, 760 01 Zlin, Czech Republic c Conducting Polymers in Composites and Applications Research Group, Faculty of Applied Sciences, Ton Duc Thang University, Ho Chi Minh City, Vietnam*

[*]*Corresponding authors at: Key Laboratory for Ultrafine Materials of Ministry of Education, Shanghai Engineering Research Center of Hierarchical Nanomaterials, School of Materials Science and Engineering, East China University of Science and Technology, 200237 Shanghai, China. E-mail addresses: rehey@ecust.edu.cn (Y. He), chengql@ecust.edu.cn (Q. Cheng).*

ABSTRACT

The battery-type anodes and capacitor-type cathodes enable lithium-ion capacitors (LICs) to achieve high energy density and high power density concurrently. Nonetheless, the gap in capacity and electrochemical reaction dynamics between anodes and cathodes remains a grand challenge. In this work, we report the synthesis of hierarchical MoS_2/C@MXene composite with uniform MoS_2/C nanosheets grown on few MXene flakes by electrostatic flocculation and hydrothermal reaction. As a result, the restacking of MXene flakes is inhibited effectively by electrostatic flocculation, and the few-layer MXene provides abundant sites for the uniform growth of MoS_2 nanosheets. Meanwhile, the amorphous carbon matrix derived from diethylenetriamine can further enhance the conductivity of MoS_2 and mitigate the oxidation of MXene. Due to the desirable coupling effect between MoS_2/C and MXene conductive networks, MoS_2/C@MXene electrode demonstrates superior Li storage capacity. It delivers a reversible capacity of 600 mAh g^{-1} at 1.0 A g^{-1} after 700 cycles, along with excellent rate performance. Moreover, the assembled LIC device using MoS_2/C@MXene as anode and threedimensional porous carbon as cathode exhibits a high energy density of 164.5 Wh kg^{-1} at the power density of 225 W kg^{-1}, and an energy density of 53.1 Wh kg^{-1} even at a high power density of 11.3 kW kg^{-1}, as well as good cycling stability with capacity retention of 77.2% after 5000 cycles at 1.0 A g^{-1}. These results indicate that MoS2/C@MXene might be promising anode materials for high-performance LICs.

Keywords: Lithium-ion capacitor, MXene MoS_2, hierarchical structure, porous carbon

1. Introduction

The ever-increasing consumption of fossil fuels has already exerted severe impact on environment, particularly as regards the air pollution and energy depletion. Therefore, exploitation and development of green energy storage devices with high energy density, high rate capability, long cycle lifespan and environmental friendliness are of crucial importance [**1-4**]. Among these devices, lithium-ion batteries (LIBs) and supercapacitors (SCs) have attracted extensive attention. LIBs are dominant in the energy storage market in view of their high gravimetric and volumetric capacity [**5,6**], while SCs are applied to many occasions for the sake of their high power density [**7,8**]. Nevertheless, both of them cannot possess the high energy density and power density simultaneously, which undoubtedly restricts their widespread applications. The key to tackle this issue is to vigorously develop advanced lithium-ion capacitors (LICs).

The electrodes of LICs are usually composed of battery-type anodes storing energy via redox reactions and capacitor-type cathodes harvesting energy by fast adsorption/desorption of ions. Due to this characteristic, LICs are also called hybrid ion capacitors and can deliver high energy density at high power density, bridging the gap between LIBs and SCs [**9,10**]. Because of great difference in energy storage mechanisms, the matching of two electrodes is an issue that cannot be ignored [**11**]. For the battery-type anode, transitional metal sulfides (TMSs) are considered to be qualified candidates owing to their high lithium storage performance [**12-14**]. Molybdenum disulfide (MoS_2) is a typical TMS with layered structure which is favorable for the diffusion of electrolyte ions, leading to superior performance in lithium storage [**15,16**]. However, there are two major drawbacks restricting the electrochemical performance of MoS_2: the poor electron conductivity and volume expansion during electrochemical reactions [**17,18**].

One of the effective strategies is to introduce conductive 2D materials as substrate which provides large quantities of active sites for the nucleation and growth of MoS_2. The substrate can not only stabilize the structure of MoS_2 during electrochemical reactions but also enhance the ability of charge transportation. Among numerous 2D conductive materials, MXene is a novel type of multi-layer transitional metal nitrides, carbides, which can be obtained by etching "A" atomic layers from the precursor MAX (M: transitional metals; A: A-group elements; X: carbon or nitrogen) with hydrofluoric acid or acid solution with high concentration of F^-. There are abundant functional groups on the surface generated during the etching process, which makes MXene a favorable substrate to load active materials [**19**]. Besides, the outstanding metallic conductivity and tunable layered structures are another two conspicuous merits for MXene [**20,21**]. Therefore, MXene has been widely applied for LIBs [**22**], Li-S batteries [**23**] and SCs [**24**].

Many previous studies have focused on the energy storage performance of MoS_2/MXene [**25-28**]. However, the 2H-MoS_2 phase in the MoS_2/MXene composite, to some extent, exerts negative effect on their electrochemical performance due to its low conductivity. To solve this problem, the 1 T-MoS_2 phase coupled with MXene have been developed and could exhibit high performance, since the 1 T phase possesses metallic conductivity [**29,30**]. However, the 1 T-MoS_2 is a type of metastable crystal according to previous report [**31**]. That is to say, it may be difficult to directly prepare 1 T-MoS_2 with high purity or completely transform 2H-MoS_2 to 1 T-MoS_2, which may make MoS_2/ MXene composite fail to achieve the expected high lithium storage performance. Consequently, it is necessary to introduce carbon matrix to address this issue, instead of directly growing MoS_2 on the surface of MXene.

In addition, some characteristics of MXene also have negative impact on performance of composite materials. Firstly, the oxidation of MXene is a non-negligible dilemma due to the oxygen containing

functional group. It is almost inevitable that TiO_2 forms in the preparation processes of composites, leading to the decrease in conductivity of MXene [**32**]. From this aspect, the introduction of carbon matrix into MoS_2/ MXene can not only increase the conductivity of MoS_2, but also make up for the negative effect caused by the oxidation of MXene. Besides, MXene flakes tends to be restacked spontaneously due to the strong van der Waals interactions between layers, giving rise to a drastic loss of their electroactive surface area and an adverse effect on the electrochemical properties [**33**]. Therefore, the essential prerequisite for improving the electrochemical performance of MXene is to reduce its self-stacking and tailor its surface properties. Recent studies have revealed that few-layer MXene flakes can possess stronger Li storage capacity than their multilayer counterparts [**34**]. Traditionally, the exfoliation of MXene flakes is realized by ultrasonic treatment and centrifugation [**35-37**] that cannot effectively break the van der Waals interaction between flakes, which often fails to address the restacking issue during preparation process. To solve this problem, a new delamination method, i.e., electrostatic flocculation approach is developed [38], which can prevent restacking of the few-layer flakes to a great extent.

With these considerations in mind, here a novel hierarchical MoS_2/ C@MXene composite is constructed. Firstly, few-layer MXene nanoflakes are obtained by ultrasonic treatment and electrostatic flocculation. Subsequently, MoS_2/C composite nanostructures are grown tightly on the surface of MXene nanosheets to form 3D MoS_2/C@MXene hierarchical structure via facile hydrothermal treatment and annealing process. The electrostatic flocculation process can break the electrostatic equilibrium between MXene flakes, thus greatly hindering the restacking. The few-layer MXene plays two crucial roles: the one is to provide a substrate with good conductivity for the construction of 3D conductive networks, and the other is to provide abundant sites for the growth of MoS_2, which may greatly alleviate the self-aggregation of MoS_2. The amorphous carbon matrix formed during the annealing process can effectively enhance the conductivity of MoS_2 and make up for the negative effect caused by the oxidation of MXene. Therefore, the novel 3D interconnected heterostructure of MoS_2/C@MXene can not only provide large electrode/electrolyte interface to reduce the distance of Li ion diffusion, but also effectively improve the electrical conductivity of composite electrode to facilitate the charge transfer. As expected, the MoS_2/C@MXene composite anode exhibits superior lithium storage performance, which outperforms than some MoS_2/MXene composites [**39-41**]. Besides, the assembled LIC based on MoS_2/C@MXene anode and 3D porous carbon cathode delivers outstanding energy density, power density and long cycling performance, indicating its great application potentiality in energy storage devices.

2. Experimental

2.1. Synthesis of few-layer Ti_3C_2 MXene

Firstly, 1.2 g Ti_3AlC_2 powder was gradually dispersed into 50 mL of HF solution (≥40%) with magnetic stirring at 50 °C for 24 h in order to etch Al atom layers. Afterwards, the black residual was collected by centrifugation. The MXene powder was then obtained by vacuum freezedrying. Secondly, the few-layer MXene was synthesized via electrostatic flocculation method. 500 mg as-prepared MXene powder was added in 20 mL TMAOH (tetramethylammonium hydroxide) solution and stirred for 24 h at room temperature, followed by centrifugation to remove organic solution. Delamination of Ti_3C_2 MXene was carried out by ultrasonic treatment of the above sediment in deionized water for 1 h under N_2 atmosphere. After that, the black supernatant was collected by centrifugation at 3500 rpm. Then, abundant NH_4HCO_3 was dissolved into 100 mL collected supernatant and let it stand for a short period of time until the flocculation phenomenon can be observed. Finally, the floccule was freeze-dried and

annealed at 180C in N_2 atmosphere for 6 h to obtain few-layer MXene powders (noted as f-MXene). Specially, in order to enhance the yield, the steps mentioned above may be taken for several times.

2.2. Synthesis of MoS_2/C@MXene

In a typical synthesis, 100 mg f-MXene powder, 1.2 g $(NH_4)_6Mo_7O_{24}$, 0.5 g CH_4N_2S were added into the solution composed of 40 mL deionized water and 20 mL diethylenetriamine (DETA) with continuous stirring. Then, the solution was transferred into 100 mL autoclave and kept for 24 h at 200 C. After the completion of hydrothermal reaction, the autoclave was naturally cooled to room temperature. The final MoS_2/ C@MXene sample was obtained by centrifugation and vacuum freezedrying, followed by annealing at 550 C for 2.5 h in N_2 atmosphere.

For comparison, the MoS_2/C composite was also synthesized under the same condition mentioned above without f-MXene powder, and the MoS2 was prepared without f-MXene powder and DETA.

2.3. Synthesis of 3D porous carbon

3D porous carbon was synthesized according to previous report with minor modification [**42**]. Generally, 1.2 g PVP (K30) and 1.6 g Fe $(NO_3)_3{\cdot}9H_2O$ were dissolved into 30 mL deionized water. The mixture was then oil-bath heated at 90 C until the water completely evaporated. Subsequently, the yellow solid residue was ground into fine powder and annealed at 650 C for 2 h in N_2 atmosphere. The black product was washed by 2.0 M HCl and deionized water for several times to obtain the final product (noted as 3D-PC).

2.4. Material characterization

The crystal structure of samples was tested via Rotating Anode X-ray Powder Diffractometer (Rigaku Corporation, Japan) (Cu Kα radiation, ↑ λ = 0.154 nm, 2θ ranges from 5° to 75°). The morphology and microstructure of specimens was respectively observed with Field Emission Scanning Electron Microscopy (FESEM, Hitachi S4800, Japan) and Transmission Electron Microscopy (TEM, JEOL JEM-2100, Japan). Energy-dispersive X-ray spectroscopy (EDS) analysis was performed by Quantax 400-30 (Beuker AXS Gmbh, Karlsruhe, Germany) adjoined to FESEM. The specific surface area of materials was measured by ASAP2460 (Micromeritics Instrument Corporation, USA) at 77 K and calculated by Brunauer-Emmett-Teller (BET) equation. X-ray photoelectron spectroscopy was conducted by K-Alpha (ThermoFisher Scientific, China) to evaluate the chemical environment of major elements in materials. Raman spectroscopy was collected by invia reflex (Renishaw, the UK) with a 532 nm wavelength laser light.

2.5. Assembly of lithium half-cell and LIC device

The lithium storage properties of MoS_2, MoS_2/C, MoS_2/C@MXene and 3D-PC was tested in CR2032 coin-type half-cells with lithium metal plates as counter electrode and glass fiber membrane as separator. The slurry was prepared by stirring mixture of active materials, super P and PVDF (8:1:1 wt% for anode, 7:2:1 wt% for cathode) for 10 h. Then the slurry was coated onto copper foil (aluminum foil for cathode) and vacuum dried at 100 °C for 12 h to form working electrode. The electrolyte was 1 M $LiPF_6$ organic solution of which solvent contained ethylene carbonate, diethyl carbonate, and dimethyl

carbonate (1:1:1 vol%). The CR2032 coin cells were assembled in a glove box filled with Argon. Before assembling the lithium-ion capacitors (LICs), the pre-lithiation process was required. CR2016 coin-type half-cells containing MoS_2/C@MXene were discharged and charged for about 10 cycles at 0.1 A g^{-1} and then discharged to 0.01 V. The fully discharged half-cell was disassembled in glove box to fetch out the anode electrode. The pre-lithiated anode electrode and 3D-PC cathode electrode were sealed into CR2032 coin cell to assemble LIC devices.

2.6. Electrochemical measurements

All electrochemical analysis was conducted at room temperature. The rate performance, galvanostatic charge/discharge (GCD) measurements and the galvanostatic intermittent titration technique (GITT) experiments were performed on LAND CT2001A battery testing system. The diffusion coefficient of electrodes was calculated by the following equation:

$$D_{Li^+} = \frac{4}{\pi\tau}\left(\frac{n_M V_M}{S}\right)^2\left(\frac{\Delta V_s}{\Delta V_\tau}\right)^2 \quad (1)$$

where the τ is the resting time, n_M is molar number, V_M is molar volume of electrode materials, S is the surface area of electrode/elec-trolyte interface, and ΔV_s, ΔV_τ represent the voltage change during the resting time and discharging process, respectively. Electrochemical impedance spectroscopy (EIS) data was investigated by applying alternative current potential 5 mV from 0.01 Hz to 100 kHz and cyclic voltammetry (CV) was recorded at various scan rates ranging from 0.01 to 3.0 V on CHI660E electrochemical station. For LICs, the potential ranged from 0 to 4.5 V. The specific capacitance of LIC was calculated by the following equation:

$$C = \frac{I \times t}{m \times (V_h - V_l)} \quad (2)$$

in which C, I, t, m, V_h, V_i represent specific capacitance, discharge current, discharging time, the mass of active material, the highest potential and the lowest potential of LIC during discharging process, respectively. Energy density (E) and power density (P) of LICs are determined by the following two equations:

$$E = \frac{1}{2}CV^2 \quad (3)$$

$$P = \frac{E}{t} \quad (4)$$

3. Results and discussion

3.1. Morphology and microstructure of MoS_2/C@MXene

Fig. 1 illustrates the preparation process of MoS_2/C@MXene composite. First, the layered $Ti_3C_2T_x$-MXene is achieved by HF etching. Then the f-MXene nanoflakes are obtained by ultrasonic exfoliation. To avoid the restacking of f-MXene sheets in the supernatant, NH_4HCO_3 is used as flocculant for effective collection of f-MXene. Due to the electrostatic interactions between negatively charged MXene flakes and positively charged ammonium ions, flocculation phenomenon takes place in a short

time. Subsequently, $(NH_4)_6Mo_7O_{24}$, CH_4N_2S and DETA are added as the source of Mo, S, and C, respectively. The MoS_2 nanosheets is deposited on the surface of f-MXene flakes and MoS_2-DETA@MXene is formed by the coordination between DETA molecules and Mo^{4+} ions during the hydrothermal reaction. After annealing treatment in N_2 atmosphere, the functional group in DETA is decomposed and transformed into amorphous carbon matrix which strongly attached with MoS_2. Finally, the MoS_2 nanosheets integrated with amorphous carbon matrix are uniformly distributed on the surfaces of single MXene flakes to form 3D MoS_2/C@MXene hierarchical architectures, which provide large quantities of channels for rapid diffusion of Li^+ ions.

The morphologies of the samples are characterized by SEM images shown in **Fig. 2** and **Fig. S1**, respectively. As indicated by **Fig. S1**c&d, the as-prepared Ti_3C_2 MXene exhibits typical accordion-like layered structure, quite different from that of Ti_3AlC_2 precursor (**Fig. S1**a &b). The separation of individual layers confirms the successful removal of Al atom layers. After ultrasonication and flocculation treatment, single flakes with width of several micrometers can be observed in SEM image of f-MXene (**Fig. 2**a). It is conspicuous that the individual flakes of Ti_3C_2 MXene can be effectively peeled off by ultrasonication and electrostatic flocculation. The restacking issue can be solved to some extent since the electrostatic equilibrium between MXene flakes has been broken by NH_4^+. **Fig. S2**b reveals that MoS_2/C almost maintains flowerlike 3D heterostructure similar to that of pure MoS_2 (**Fig. S2**a). The elementary mapping (**Fig. S3**a) shows the distribution of Mo, S and C, indicating the existence of carbon matrix after decomposition of function groups of DETA. The carbon in MoS_2/C can improve the electrical conductivity of composites to enable rapid charge transfer. Note that a certain degree of agglomeration occurs in both MoS_2 and MoS_2/C, which may reduce their contact area with the electrolyte, exerting negative impact on their lithium storage performance. **Fig. 2**b demonstrates that the MoS_2/C subunits ranging from 200 to 300 nm are perpendicularly and uniformly grown on the surface of single Ti_3C_2 flakes. The elementary mapping (**Fig. S3**b) shows the uniform distribution of Ti, C, Mo, S. Due to the relatively large lateral size of f-MXene, the separated MXene flakes offer adequate sites for nucleation and growth of MoS_2/C, which obviously alleviates the aggregation of MoS_2/C (**Fig. 2**c).

To further investigate the microstructure of MoS_2/C@MXene, TEM is performed. As shown in **Fig. 2**d, the flower-like MoS_2/C with the lamellar thickness less than 10 nm are uniformly inserted in f-MXene flakes, which is in line with SEM images in **Fig. 2**b. High resolution TEM (HRTEM) images (**Fig. 2**e&f) indicates that MoS_2/C exhibits typical layered structure and the mean value of interlayer spacing between individual MoS_2 nanosheets is around 0.64 nm. The TEM results clearly substantiate the successful synthesis of MoS_2/C@MXene composite with interconnected 3D structure. The f-MXene flakes with ultra-thin nanosheets on the surface can promote transfer of ions and electron and shorten the diffusion path of ions [**43,44**].

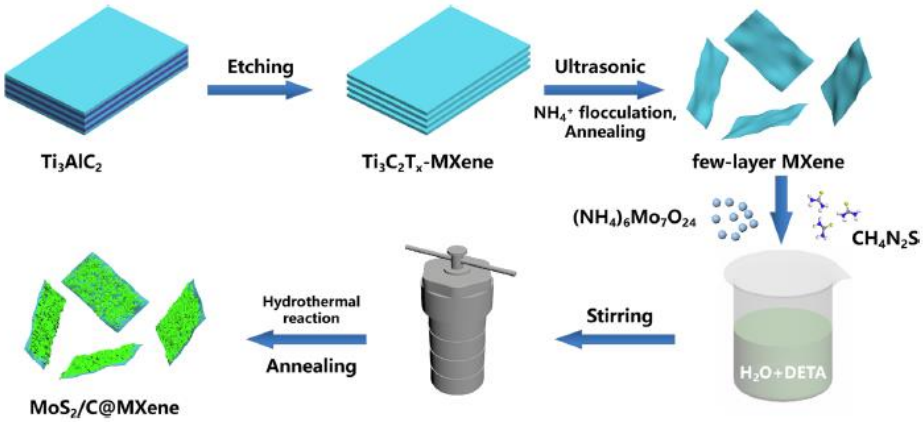

Fig. 1. Schematic diagram of synthesis process of MoS_2/C@MXene.

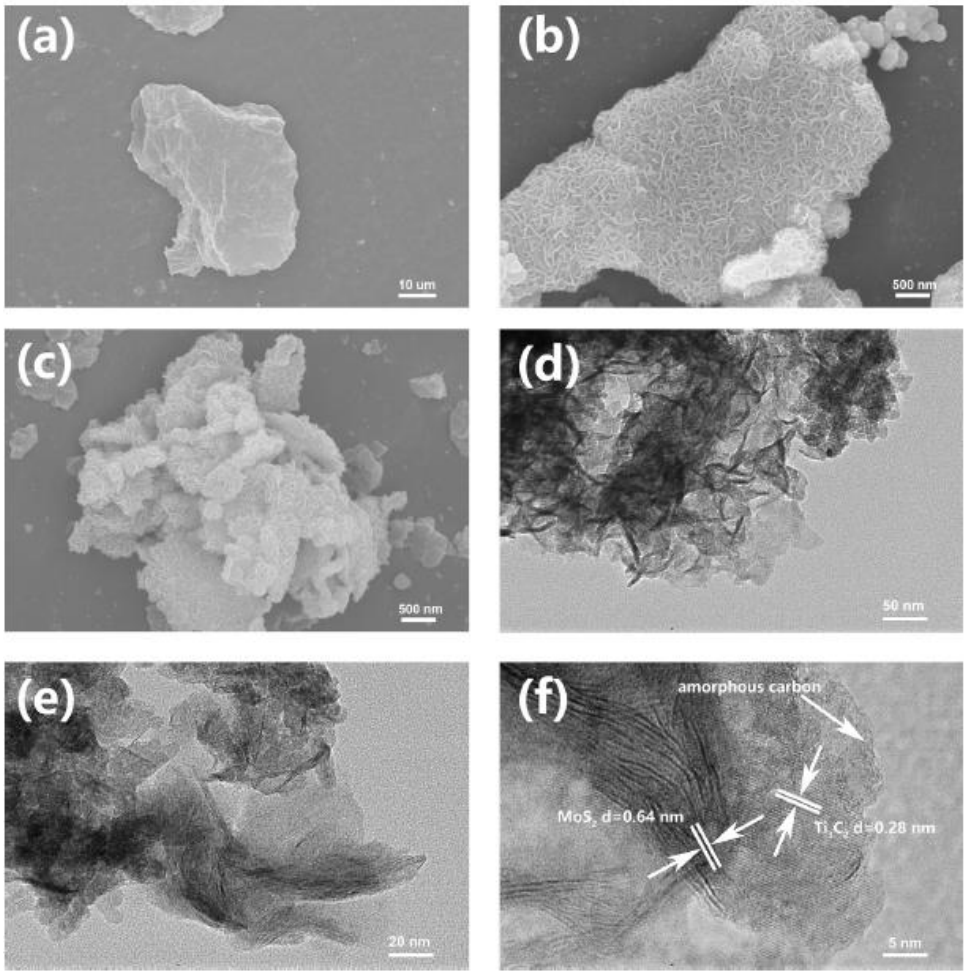

Fig. 2. SEM images of (a) f-MXene and (b, c) MoS_2/C@MXene; (d-f) TEM images of MoS_2/C@MXene at different magnifications.

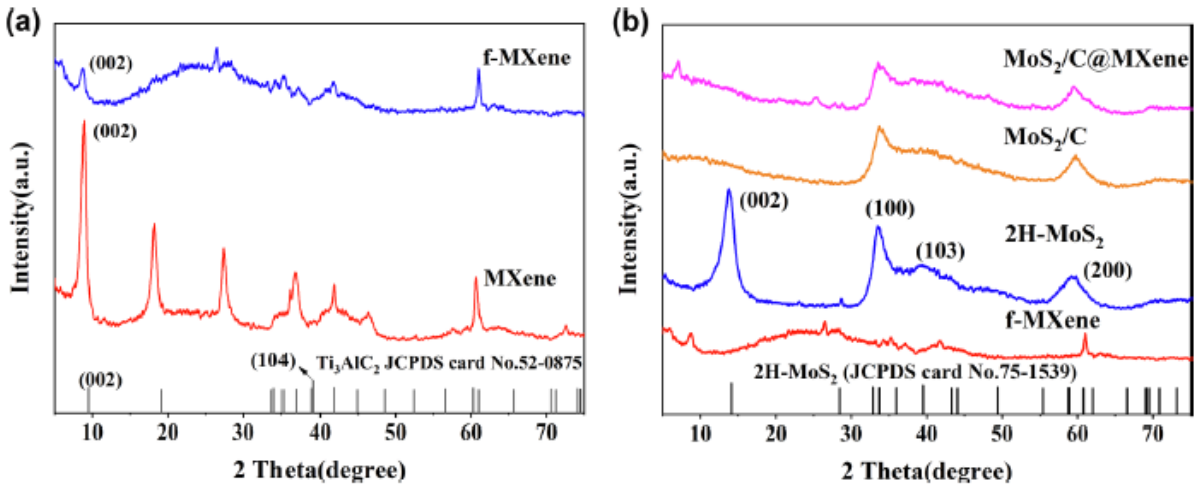

Fig. 3. XRD patterns of (a) MXene, f-MXene and (b) f-MXene, 2H-M0S_2, M0S_2/C and MoS_2/C@MXene.

The crystal structure of composites is analyzed by XRD patterns (**Fig. 3**). As shown in **Fig. 3**a, the (104) peak at 2θ ≈ 39° of Ti_3AlC_2 (JCPDS card No.52-0875) can hardly be detected in diffraction pattern of Ti_3C_2 MXene and f-MXene, which verifies the successful removal of Al atom layers. The (002) peaks for f-MXene, MXene and Ti_3AlC_2 appear at around 8.68°, 8.90°, 9.52°, corresponding to the d-spacing values of 10.11 nm, 9.82 nm and 9.29 nm, respectively. That is to say, f-MXene has relatively larger interlayer spacing in favor of fast penetration of electrolyte. Fig. 3b shows the diffraction peaks at 13.8°, 33.5°, 39.4°, 59.3° attributed to (002), (100), (103), (110) crystal planes of 2H-MoS_2 (JCPDS card No.75-1539). In contrast, the strong peak (002) at 13.8° of MoS_2 almost vanishes in the patterns of MoS_2/C and MoS_2/ C@MXene, which could be caused by the shielding effect of amorphous carbon matrix [**45**]. The other characteristic peaks of MoS_2/C and f-MXene can be detected in the pattern of MoS_2/C@MXene, indicating successful combination of two phases in the composite. More importantly, the (002) peak of MoS_2/C@MXene is shifted to 6.93°, lower than that of f-MXene, which strongly suggests that MoS_2/C can further expand interlayer spacing of f-MXene and effectively prevent the restacking of MXene layers.

XPS technology was carried out to analyze the chemical circumstance of elements (**Fig. 4**). The general spectrum in **Fig. 4**a indicates the coexistence of C, O, S, Ti and Mo. High-resolution XPS spectrum of Ti 2p (Fig. 4b) is deconvoluted into four pairs of couplet peaks: Ti^{2+} with binding energy of 456.2 eV and 461.5 eV, Ti^{3+} with binding energy of 458.5 eV and 463.6 eV, Ti-O with binding energy of 459.2 eV and 464.8 eV, and Ti-C with binding energy of 455.6 eV and 460.6 eV [**46**]. The Ti-O peaks indicate the presence of oxygen-containing group on the surface of Ti_3C_2 layers. In **Fig. 4**c, the Mo $3d_{3/2}$ (Mo-S bond) at 232.8 eV and Mo $3d_{5/2}$ (Mo-S bond) at 229.6 eV are observed in the spectrum of Mo 3d. Besides, the peak at 226.7 eV originates from S 2p of MoS_2, confirming the existence of MoS_2 phase in MoS_2/C@MXene. The peaks at 229.1 eV and 232.1 eV may be attributed to Mo-C bond, demonstrating the interaction between MoS_2 and amorphous carbon matrix. The peak at 235.7 eV is related to Mo6+, indicating the partial surface oxidation of MoS_2 [**28,47**]. A pair of couplet peaks at 163.5 eV and 162.3 eV, as shown in **Fig. 4**d, belong to S $2p_{1/2}$ and S $2p_{3/2}$, respectively [**48**]. In the spectrum of O 1 s (**Fig. 4**e), four peaks centered at 530.2 eV, 531.0 eV, 532.4 eV and 533.5 eV represent TiO_2, C-Ti-O, C-Ti-$(OH)_x$ and H_2O_{ad} (adsorbed water), respectively [**49**]. The spectrum of C 1 s (**Fig. 4**f) exhibits three peaks: C-Ti-O peak at 284.3 eV, C-C peak at 284.8 eV and CO peak at 286.2 eV [**50**]. The C-C bond also strongly confirms the fact that MoS_2/C@MXene contains the amorphous carbon matrix.

Raman spectra was also applied to characterize the surface structure of MoS_2/C@MXene. As illustrated in **Fig. 5**a, the peak at 150.8 cm^{-1} represents the vibration of Ti_3C_2, which is caused by E_g^1 vibration mode of anatase [**51**]. The two obvious peaks are ascribed to the vibration of 2H-MoS_2 phase. Specially, the peak at 373.8 cm^{-1} represents the E^1_{2g} vibrational mode (in-plane vibrational mode) and the one at 400.4 cm^{-1} represents the A_{1g} vibrational mode of molybdenum disulfide molecules [**52**]. Meanwhile, the D-band and G-band located at 1370.5 cm^{-1} and 1578.4 cm^{-1} are the symbol of disordered carbon and graphene carbon, respectively. The ratio of peaks intensity of D-band to G-band, ID/IG, is around 0.93, very close to 1.0. This result is evidence for the existence of amorphous carbon in composite, which is in good agreement with the results of TEM, XRD and XPS. **Fig. 5**b depicts the N_2 adsorption/ desorption isothermal curves of MoS_2/C and MoS_2/C@MXene. The isothermal curve of MoS_2/C@MXene is typical type II shape with obvious H3-type hysteresis loops, indicative of the predominant meso-porosity for MoS_2/C@MXene [**53**]. The corresponding pore size distribution results (inset in **Fig. 5**b) shows the large number of pores ranging from ~ 3 to 10 nm. In contrast, MoS_2/C exhibits obviously less N_2 adsorption quantity than MoS_2/C@MXene. The specific surface area (SSA) of MoS_2/C@MXene and MoS_2/C are 25.02 $m^2\ g^{-1}$ and 9.50 $m^2\ g^{-1}$, respectively. The larger SSA of MoS_2/C@MXene is the powerful evidence that f-MXene flakes can provide numerous sites for the growth of MoS_2 sheets, thus effectively reducing the agglomeration of MoS_2. The high SSA could increase the active sites for electrochemical reaction, resulting in an improved Li^+ storage performance.

3.2. Electrochemical properties of MoS2/C@MXene anode

The electrochemical performance of MoS_2/C@MXene anode was evaluated in CR2032 coin cells with metal lithium plates as counter electrode. CV test was conducted at 0.1 mV s^{-1} with voltage ranging from 0.01 to 3.00 V and the curves are presented in **Fig. 6**a. In the first cathodic scan, the peak at 1.05 V corresponds to intercalation of Li^+ into the lattice of MoS_2 to form the compound $LixMoS_2$ [**54**]:

$$xLi^+ + MoS_2 + xe^- \rightarrow Li_xMoS_2 \quad (5)$$

The following reduction peak at around 0.56 V indicates the conversion of Li_xMoS_2 to Li_2S and metal Mo:

$$Li_xMoS_2 + (4-x)Li^+ + (4-x)e^- \rightarrow 2Li_2S + Mo \quad (6)$$

In the first anodic sweep, the weak peak at 1.61 V is oxidation of Mo:

$$2Li_2S + Mo \rightarrow MoS_2 + 4Li^+ + 4e^- \quad (7)$$

The subsequent strong oxidation peak at about 2.25 V denotes that Li_2S is delithiated and converts to Li^+ and S [**55**]:

$$Li_2S \rightarrow 2Li^+ + S + 2e^- \quad (8)$$

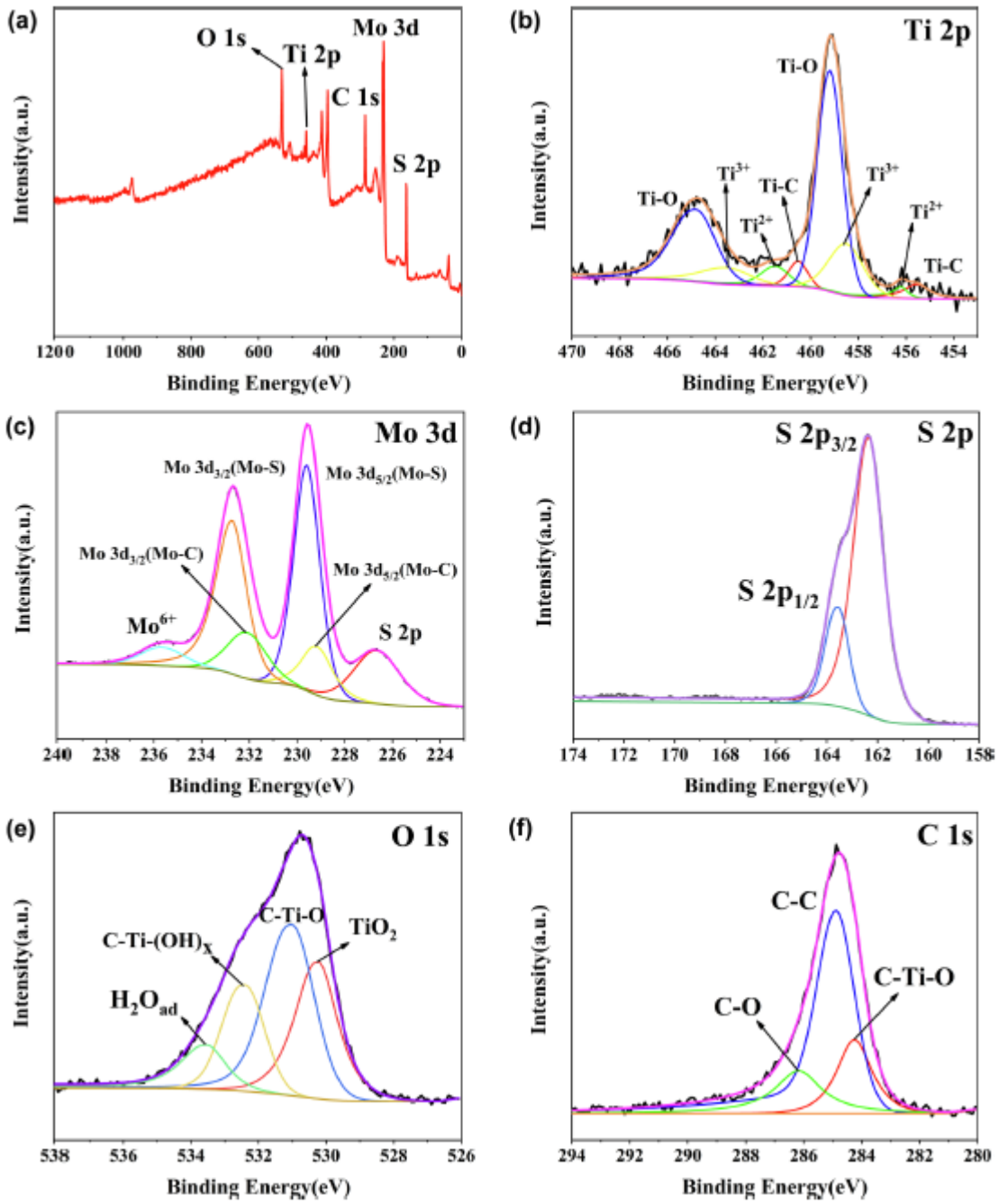

Fig. 4. XPS characterization of MoS_2/C@MXene: (a) total spectrum; high-resolution spectra of (b) Ti 2p, (c) Mo 3d, (d) S 2p, (e) O 1 s and (f) C 1 s.

During the next three scan cycles, the peak at 0.56 V diminishes because the solid-electrolyte interface (SEI) has already formed and Li^+ is irreversibly deintercalated during the 1st cathodic scan. The reduction peak at 1.9 V is the formation of Li_2S [**55**]:

$$2Li^+ + S + 2e^- \rightarrow Li_2S \qquad (9)$$

The highly overlapping curves for 2nd, 3rd and 4th charge/discharge scans suggest the excellent electrochemical reversibility and stability of MoS_2/C@MXene. The GCD profiles at a current density of 0.1 A g^{-1} are exhibited in the **Fig. 6**b. The voltage plateaus in GCD curves match very well with CV

diagram. The shape of curves for four discharge/charge cycles, except the 1st discharging process for the sake of irreversible reaction related to the formation of SEI, almost remain unchanged, demonstrating the stability of the anode material.

To compare the lithium storage performance of MoS_2, MoS_2/C and MoS_2/C@MXene, cycling and rate performance are conducted at different current densities. **Fig. 6**c demonstrates the cycling stability of MoS_2/C@MXene at 1.0 A g^{-1}. In the initial cycles, the capacity declines in first 50 cycles and gradually increases in subsequent discharging/ charging cycles.

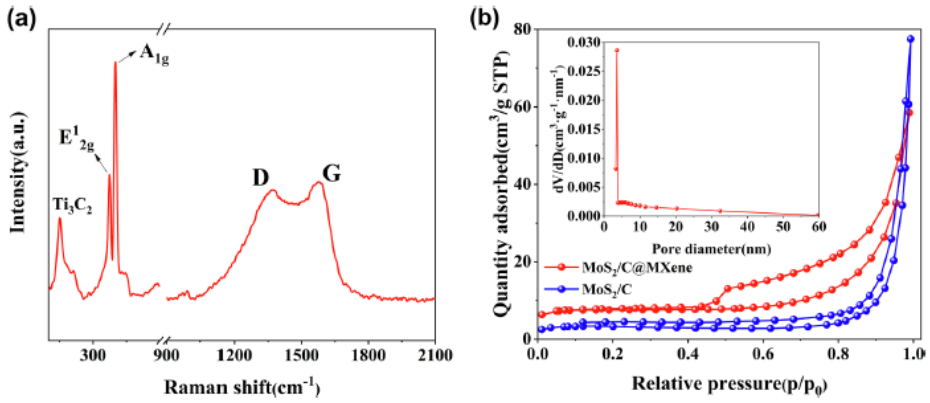

Fig. 5. (a) Raman spectra of MoS_2/C@MXene. (b) N_2 adsorption/desorption isothermal curves and of MoS_2/C@MXene and MoS_2/C. Inset: pore size distribution of MoS_2/C@MXene.

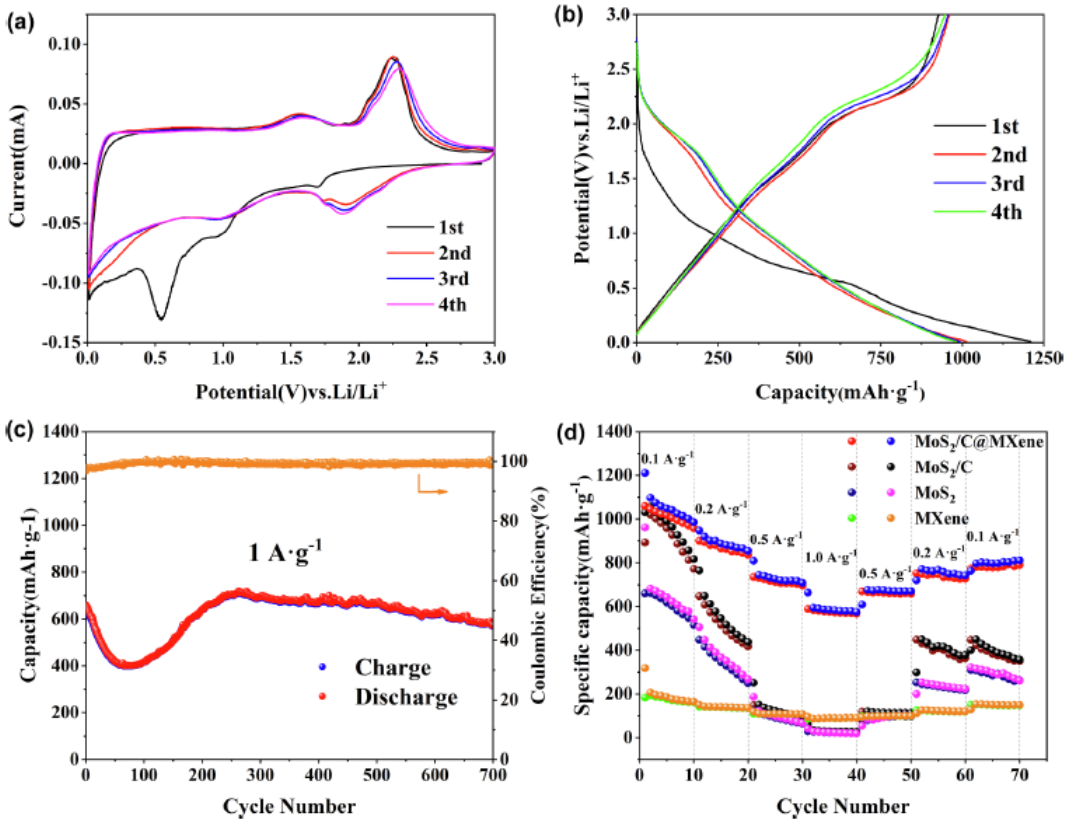

Fig. 6. (a) CV curves of MoS_2/C@MXene at 0.1 mV s^{-1}; (b) GCD curves of MoS_2/C@MXene at 0.1 A g^{-1}; (c) cycling performance of MoS_2/C@MXene at 1.0 A g^{-1}; (d) rate performance of MoS_2, MoS_2/C and MoS_2/C@MXene at various current density between 0.1 and 1.0 A g^{-1}.

This might be caused by the activation process of electrode materials and the gradual electrolyte infiltration. In the initial stages of cycling test, the formation of SEI layers occurs. The SEI may break and reform during first 50 cycles, giving rise to the consumption of lithium ions. Therefore, an obvious loss in specific capacity can be detected. After this stages, the stable SEI layers are formed, and more active materials are exposed to make good contact with electrolyte. That is to say, the lithium-ion accessibility of MoS_2/C@MXene electrode is significantly improved, and thus the capacity gradually increases. This phenomenon is also similar to some other electrode materials [**56-58**]. It can be found that the MoS_2/C@MXene electrode delivers a high reversible capacity of 600 mAh g^{-1} and its coulombic efficiency remains a value very close to 100%, indicating its outstanding cycling performance. In addition, the SEM of MoS_2/C@MXene after cycling stability test (**Fig. S4**b) almost maintains its original morphology (**Fig. S4**a), further confirming its structural stability during the electrochemical reaction. According to **Fig. 6**d, in first cycle, the discharge and charge capacity of the MoS_2/C@MXene electrode is 1210 mAh g^{-1} and 1059 mAh g^{-1}, respectively. The coulombic efficiency is 87.5% in the initial cycle because of the formation of SEI. MoS_2/C@MXene electrode subsequently delivers capacity about 1000, 890, 710, 575 mAh g^{-1} at 0.1, 0.2, 0.5 and 1.0 A g^{-1}, respectively. As current densities gradually return to 0.5, 0.2 and 0.1 A g^{-1}, the capacities are 670, 750 and 810 mAh g^{-1} without significant decrease. At each current density, the capacity of MoS_2/C@MXene almost remains unchanged. By contrast, a remarkable capacity decline can be observed for MoS_2/C and MoS_2 at 0.1 A g^{-1}. When current density increases up to 1.0 A g^{-1}, these two electrodes can only exhibit quite low capacity ($<$ 100 mAh g^{-1}). The superior rate performance of MoS_2/C@MXene may be attributed to its hierarchical structure—MXene, as a substrate with high conductivity, can act as a buffer to alleviate the volume expansion during electrochemical reaction processes. Also, uniformly distributed nanosheets on the surface of f-MXene flakes lead to shorter diffusion paths of ions, beneficial for the higher lithium storage performance [**59**].

In order to reveal the reaction dynamics of electrodes, EIS measurements were conducted. **Fig. S5** shows the Nyquist plots of pure MoS_2, MoS_2/C and MoS_2/C@MXene. The two intercepts on the real axis are R_s (bulk electrolyte resistance) and $R_s + R_{ct}$ (R_{ct}, charge transfer resistance), respectively [**60**]. Clearly, all of the three electrodes almost share the same R_s value (~1.6 Ω), but they exhibit different R_{ct}. The MoS_2/C@MXene electrode has the lowest R_{ct} (~50 Ω) while the R_{ct} of MoS_2/C electrode is around 160 Ω, lower than that of pure MoS_2 electrode (~400 Ω). Lower R_{ct} of MoS_2/C exactly illustrates the role of carbon matrix produced by the decomposition of DETA after annealing. The lowest R_{ct} of MoS_2/C@MXene verifies the fact that the introduction of MXene can further enhance the charge transfer kinetics. In addition, the inclined straight line in the low frequency region is related to the lithium-ion diffusion of electrode materials and the larger slope signifies more excellent lithium-ion diffusion dynamics [**61**]. The relatively larger slope of straight line for MoS_2/C@MXene reflects its faster Li-ion diffusion rate, which may be attributed to the large quantity of porosity facilitating the transfer of ions in electrolyte, as illustrated in **Fig. 5**b.

To further understand the lithium storage mechanism and electrochemical dynamics, CV curves at various scan rates are listed in **Fig. 7**a. As the scanning rate gradually increasing from 0.2 to 2.0 mV s^{-1}, all the curves almost keep the same shape, except for a slight shift of the peak positions due to the polarization, which reveals the superior electrochemical reversibility and stability of the MoS_2/C@MXene electrode. The relation between the current of redox peaks and scan rate can be described by the power law:

$$i = av^b \tag{10}$$

where the parameter a and b are empirical constant. The equation can be transformed to logarithmic form:

$$log(i) = log(a) + blog(v) \quad (11)$$

The b-value can be derived from the slope of the linear fitting line of log(i) vs. log(v). As the b-value equals 0.5, the energy storage is dominated by diffusion-controlled behavior; while it is 1.0, the energy storage is dominated by capacitive behavior [62]. The results of linear fitting are listed in **Fig. 7**b. The b-value for two anodic and cathodic peaks are 0.86, 0.68, 0.87, 0.87, respectively. All the values are between 0.5 and 1.0, manifesting that both diffusion-controlled behavior and capacitive behavior participate in the energy storage process of MoS_2/ C@MXene electrode. To analyze the contribution of these two behaviors in energy storage process quantitively, another equation describing relations between current i and scan rates v is applied:

$$i = k_1 v + k_2 v^{\frac{1}{2}} \quad (12)$$

The $k_1 v$ and $k_2 v^{1/2}$ represents the capacitive and diffusion-controlled contribution, respectively [**63**]. The equation can be transformed to the following equation to determine the value of k_1 and k_2:

$$i/v^{\frac{1}{2}} = k_1 v^{\frac{1}{2}} + k_2 \quad (13)$$

The CV curve at 1.0 mV s^{-1} is shown in **Fig. 7**c. According to calculation, the capacitive behavior contribution part (the red area) accounts for about 73.12%. The ratio of capacitive behavior contribution to total energy storage behavior at 0.2, 0.4, 0.6, 0.8 and 1.0 mV s^{-1} are 53.01%, 57.15%, 63.85%, 68.19% and 73.12%, respectively, as listed in **Fig. 7**d. As the scan rate gradually increases, the capacitive behavior dominates the energy storage process, which may be ascribed to the combination of amorphous carbon matrix and MXene. The larger ratio of capacitive behavior contribution indicates more rapid ion transportation and reaction kinetics for MoS_2/C@MXene, which makes it a suitable candidate for anode materials of LICs.

Galvanostatic intermittent titration technique (GITT) was also measured to further study the lithium-ion diffusion ability of MoS_2, MoS_2/C and MoS_2/C@MXene anodes. **Fig. 7**e describes the relations between discharge voltage and specific capacity at 0.1 A g^{-1} with discharging for 10 min and resting for 60 min. The corresponding Li^+ diffusion coefficients (DLi^+) are plotted in the **Fig. 7**f. It can be found that the diffusion coefficients of all samples are in the same order of magnitude, but the value of DLi^+ for MoS_2/C@MXene is larger than that of MoS_2/C and MoS_2. The result quantitively confirms that the 3D interconnected heterostructure of MoS_2/C@MXene can effectively enhance the diffusion rate of Li^+, thus resulting in better electrochemical performance.

3.3. Structural and electrochemical properties of porous carbon cathode

The preparation process of 3D porous carbon (3D-PC) is illustrated in **Fig. S6**, and its morphology is characterized in **Fig. S7**a. It is evident that 3D-PC displays loose and porous network structure with large amount of interlaced nanosheets, which are beneficial for fast immersion of electrolyte. The Raman spectrum shown in Fig. S7b reveals that the intensity ratio of D-band (1366.7 cm^{-1}) to G-band (1587.6 cm^{-1}) is around 1.01, demonstrating the dominantly disordered carbon in 3D-PC. **Fig. S7**c presents the N_2 adsorption/desorption isothermals and pore size distribution curves. As illustrated in inset in **Fig. S7**c, 3D-PC has the specific surface area (SSA) of 1396.71 m^2 g^{-1} with large quantities of

mesopores. The interconnected 3D framework with large SSA and high porosity enables fast transportation of ion. The pore size distribution of 3D-PC (inset of **Fig. S7**c) indicates that the pore size centered at 1.5-4 nm, which falls within the size of solvated PF_6, can lead to the desired capacitance of 3D-PC.

The electrochemical performances of 3D-PC based half-cell are tested in the CR2032 coin cell with metal Li as counter electrode and the results are listed in **Fig. 8** and **Fig. S8**. The **Fig. S8** shows the CV curves of 3D-PC from 3.0 to 4.5 V at a series of scan rates. All curves present the typical quasi-rectangular shape.

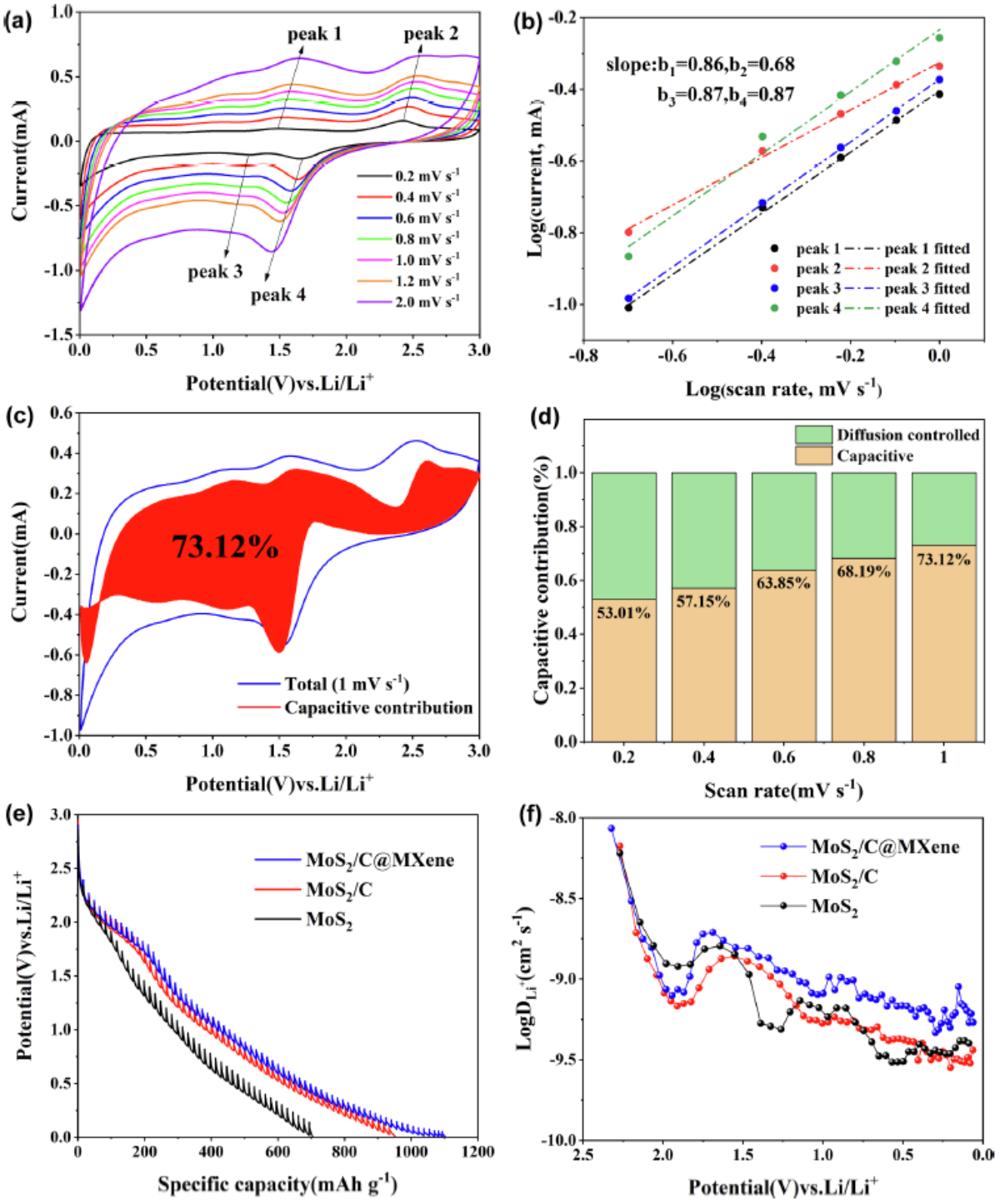

Fig. 7. (a) CV curves of MoS_2/C@MXene at different scan rates; (b)The relation between peak current and scan rates from 0.2 to 1.0 mV s^{-1} for MoS2/C@MXene electrode; (c) CV curve of MoS_2/C@MXene at 1.0 mV s^{-1} with calculated contribution

of capacitive behavior (red area); (d) The ratio of capacitive contribution from 0.2 to 1.0 mV s^{-1}. (e) Discharge GITT profiles (discharging time: 10 min; resting time: 60 min) and (f) Li-ion diffusion coefficients of MoS_2, MoS_2/C and MoS_2/C@MXene.

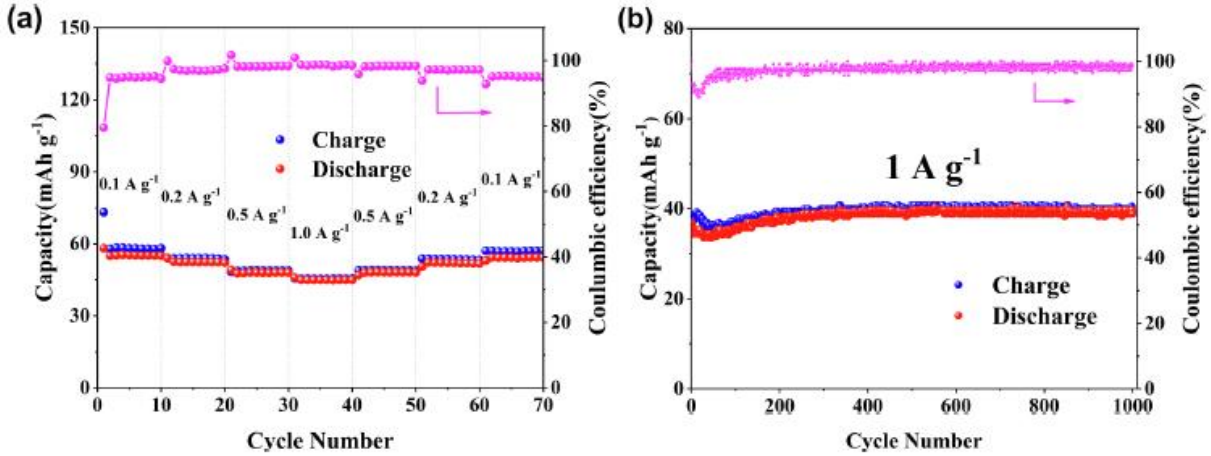

Fig. 8. (a) Rate performance of 3D-PC. (b) Cycling performance of 3D-PC at 1 A g^{-1}.

The shape does not deviate too much even at a high scan rate of 100 mV s^{-1}, reflecting the stable capacitive characteristics of 3D-PC. As shown in **Fig. 8**a, the 3D-PC cathode possesses the reversible capacity of about 60, 53, 48, 43 mAh g^{-1} at 0.1, 0.2, 0.5, 1.0 A g^{-1}. There is no obvious decay in capacity as the current density goes back to 0.1 A g^{-1}, showing the excellent rate performance of 3D-PC. Furthermore, the long cycling life test at 1.0 A g^{-1} (**Fig. 8**b) shows that 3D-PC electrode can deliver stable and reversible capacity of 40 mAh g^{-1} with nearly 100% Coulombic efficiency during 1000 cycles. The outstanding electrochemical performance verifies the fact that as-prepared 3D-PC exhibits stable capacitive characteristics, fast reaction dynamics and high reversible capacity at different current densities. What's more, owing to high performance at 3.0-4.5 V, it can expand the voltage range of full-cell when used as cathode, which is significant for achieving higher energy density at given power density. Therefore, 3D-PC is a qualified candidate for cathode materials of LICs.

3.4. Electrochemical performance of MoS_2/C@MXene//3D-PC LIC

The LIC was assembled in CR2032 coin cell with MoS_2/C@MXene composites as anode and 3D-PC as cathode in 1 M $LiPF_6$ electrolyte, as depicted in schematic diagram in **Fig. 9**a. In the charging process, Li^+ ions in the electrolyte are intercalated into MoS_2/C@MXene anode. Meanwhile, the rapid adsorption of PF_6 occurs on the surface of 3D-PC cathode. During the discharging process, deintercalation of Li^+ and desorption of PF^-_6 occurs in the anode and cathode, respectively. To set the suitable voltage window for the LIC device, the CV test at different voltage ranges was conducted (**Fig. S9**). The LIC device can maintain the typical pseudocapacitive characteristic at 4.5 V. Therefore, the highest voltage exerting on the full-cell is 4.5 V. Due to the imbalance in electrochemical reaction dynamics between MoS_2/C@MXene anode and 3D-PC cathode, a suitable mass ratio of active materials of two electrodes is an important parameter for LIC to achieve excellent properties. The mass ratio can be theoretically calculated by $m_{anode}Q_{anode} = m_{cathode}Q_{cathode}$, where m denotes the mass loading of electrodes and Q represents the specific capacity. But owing to the slower reaction dynamics of battery-type anode, it is necessary to choose higher ratio of mass loading for anode in order to narrow the gaps in reaction dynamics between the anode and cathode. Based on this analysis, the mass ratios ranging from 1:2 to 1:4 were tested. According to **Fig. S10**, the LIC delivers the best

performance when the active materials mass ratio of anode to cathode is 1:2.5. The subsequent test is conducted based on this mass ratio.

As shown in **Fig. 9**b, the CV curves of MoS_2/C@MXene//3D-PC LIC at various scan rates from 0 to 4.5 V maintain quasi-rectangular shape, indicating the coupling effect of the different charge storage mechanism for both electrodes of LIC device. Additionally, the GCD curves (**Fig. 9**c) at different current density exhibit approximately symmetrical triangular shape, confirming that the different charge storage mechanism is matched and combined within MoS_2/C@MXene//3D-PC LIC. As illustrated in **Fig. 9**d, the specific capacitance of the LIC device is 58.24F g^{-1} at 0.1 A g^{-1}. The device can still hold the specific capacitance of $\sim$ 19F g^{-1} even at 5.0 A g^{-1}. Besides, the long cycling stability is also performed at 1.0 A g^{-1} shown in **Fig. 9**e. The device can retain about 77.2% of capacitance retention after 5000 charging/discharging cycles, along with a perfect Coulombic efficiency, showing impressive cycling stability of MoS_2/C@MXene//3D-PC LIC, which is also better than or closed to some reported LICs based on MoS_2 [**64-66**]. **Fig. S11** a&b display the Nyquist plot and Bode plot of the LIC device, respectively. The R_{ct} of MoS_2/C@MXene//3D-PC LIC is only 20 Ω, after the completion of CV and GCD test, the R_{ct} of MoS_2/C@MXene//3D-PC LIC only rises to 40 Ω (**Fig. S11**c), demonstrating its excellent charge transfer dynamics. The Bode plot explicates the relation between phase angle and frequency. In accordance with previous reports [**67,68**], the phase angle located at 0.01 Hz is related to the energy storage mechanism. The larger phase angle at the tail indicates the capacitive-dominated behavior during energy storage process. For an ideal capacitor, this value equals 90°, but that of MoS_2/C@MXene//3D-PC LIC at 0.01 Hz is 77°, implying that pseudocapacitive behavior is dominant energy storage mechanism for the LIC device. This is also another proof for the good matching between anode and cathode.

Fig. 9f presents the Ragone plot of MoS_2/C@MXene//3D-PC LIC and previously reported device. The energy density and power density are determined by eq. (3) and (4). At the power density of 225 W kg^{-1}, the MoS_2/C@MXene LIC device achieves an energy density of 164.5 Wh kg^{-1}. Even at a high power density of 11.3 kW kg^{-1}, it can still reach up to 53.1 Wh kg^{-1}. The energy density surpasses that of other LIC systems, such as $Ti_3C_2T_x$/CNTs//AC [**69**], $MoSe_2$//AC [**70**], CoS//FCS [**71**], TiS_2//AC [**72**], Nb_3O_7F//AC [**73**], Nb_2O_5//PSC [**74**], 3D-PCNF/MoS_2-NFFBs//AC [**68**], MnO@C//PC [**75**]. What's more, this assembled LIC device can provide power for an electronic thermometer to complete the temperature measurement (**Fig. S12**). The superior performance of the MoS_2/C@MXene//3D-PC LIC can be ascribed to the following advantages: (1) The MoS_2/C@MXene electrode deliver high reversible capacity with outstanding durability at different current densities. The low charge transfer resistance and large contribution of capacitive behavior endow it with rapid electrochemical reaction kinetics. These merits make MoS_2/C@MXene suitable for anode of LICs; (2) The porous framework of 3D-PC offers Li^+ with large quantities of channels for its transportation, thus leading to fast adsorption/desorption of ions and exhibiting typical pseudocapacitive energy storage mechanism. It can also expand the voltage window of LICs for its superior performance at 3.0-4.5 V. These advantages make the 3D-PC quite a qualified candidate for cathode of LICs; (3) An optimized active materials mass ratio of anode to cathode can fill the gap of electrochemical reaction kinetics between two electrodes to the great extent, thus exhibiting superb matching in reaction dynamics.

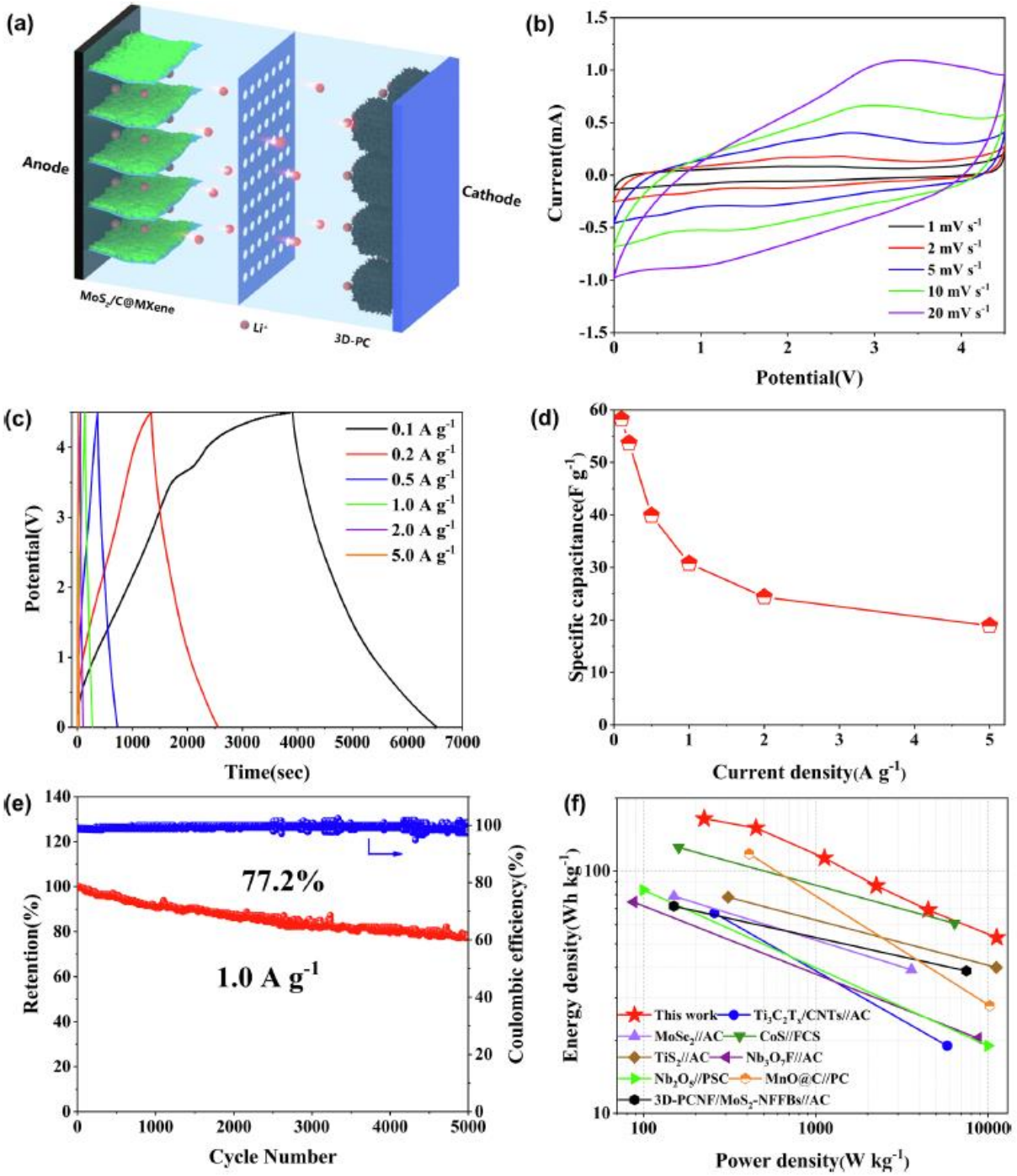

Fig. 9. (a) Schematic diagram of MoS_2/C@MXene//3D-PC LIC. (b) CV curves at different scan rates. (c) GCD curves at different current densities. (d) Specific capacitance at different current densities. (e) Long cycling performance at 1.0 A g^{-1}. (f) Ragone plot of MoS_2/C@MXene//3D-PC LIC (compared with some previously reported devices).

4. Conclusion

In summary, the f-MXene flakes are successfully exfoliated through ultrasonic and electrostatic flocculation method, followed by facile hydrothermal reaction and annealing to synthesize MoS_2/C@MXene with hierarchical composite structure. The restacking of MXene is prevented by electrostatic flocculation since the electrostatic equilibrium between the flakes is broken by flocculant NH_4^+. The f-MXene flakes provide abundant surface sites for nucleation and growth of MoS_2, thus preventing agglomeration of MoS_2 and creating large quantities of channels for diffusion of Li^+ ions.

The amorphous carbon matrix derived from DETA can further enhance the conductivity of MoS_2 and prevent the oxidation of MXene. Due to the coupling effect of MoS_2/C and MXene, the composite electrode can achieve high reversible capacity and retain about 600 mAh g^{-1} after 700 cycles at 1.0 A g^{-1}. The composite electrode shows lower R_{ct} than MoS_2 electrode, indicating that MXene flakes and carbon matrix originated from the decomposition of DETA can significantly decrease the resistance of electrode. The 3D-PC with three-dimensional connected porous framework is also prepared as cathode and displays good lithium storage performance with typical capacitive behavior. The MoS_2/C@MXene//3D-PC LIC device is assembled based on these as-prepared electrode materials. The LIC device exhibits the desired synergetic effect of anode and cathode with outstanding electrochemical performance. It delivers 164.5 Wh kg^{-1} at the power density of 225 W kg^{-1}, and 53.1 Wh kg^{-1} even at high power density of 11.3 kW kg^{-1}. Also, the device retains 77.2% of initial capacity at 1.0 A g^{-1} after 5000 charging/discharging cycles. The excellent lithium storage properties and optimized mass ratio of active materials of two electrodes are two major factors for achieving superior performance for LIC devices, indicating its great potential applications in future energy storage areas.

References

[1] Y. Zhu, Y. Huang, M. Wang, Three-dimensional hierarchical porous MnCo2O4@ MnO2 network towards highly reversible lithium storage by unique structure, Chem. Eng. J. 378 (2019), 122207.

[2] C.-F. Cheng, X. Li, K. Liu, F. Zou, W.-Y. Tung, Y.-F. Huang, X. Xia, C.-L. Wang, B. D. Vogt, Y. Zhu, A high-performance lithium-ion capacitor with carbonized NiCo2O4 anode and vertically-aligned carbon nanoflakes cathode, Energy Storage Mater. 22 (2019) 265-274.

[3] Q. Li, D. Li, K. Zhao, L. Wang, K. Wang, State of health estimation of lithium-ion battery based on improved ant lion optimization and support vector regression, J. Energy Storage 50 (2022), 104215.

[4] Z. Cui, L. Wang, Q. Li, K. Wang, A comprehensive review on the state of charge estimation for lithium-ion battery based on neural network, Int. J. Energy Res. 46 (2022) 5423-5440.

[5] L. Yu, X. Zhou, L. Lu, X. Wu, F. Wang, Recent developments of nanomaterials and nanostructures for high-rate lithium ion batteries, ChemSusChem 13 (2020) 5361-5407.

[6] Y. Zhao, X. Li, B. Yan, D. Xiong, D. Li, S. Lawes, X. Sun, Recent developments and understanding of novel mixed transition-metal oxides as anodes in lithium ion batteries, Adv. Energy Mater. 6 (2016) 1502175.

[7] C. Huang, Y. Ding, C. Hao, S. Zhou, X. Wang, H. Gao, L. Zhu, J. Wu, PVP-assisted growth of Ni-Co oxide on N-doped reduced graphene oxide with enhanced pseudocapacitive behavior, Chem. Eng. J. 378 (2019), 122202.

[8] J. Jiang, Y. Zhang, Y. An, L. Wu, Q. Zhu, H. Dou, X. Zhang, Engineering ultrathin MoS_2 nanosheets anchored on N-doped Carbon microspheres with pseudocapacitive properties for high-performance lithium-ion capacitors, Small Methods 3 (2019) 1900081.

[9] B. Li, J. Zheng, H. Zhang, L. Jin, D. Yang, H. Lv, C. Shen, A. Shellikeri, Y. Zheng, R. Gong, J.P. Zheng, C. Zhang, Electrode materials, electrolytes, and challenges in nonaqueous lithium-ion capacitors, Adv. Mater. 30 (2018) 1705670.

[10] Y. Kim, S.C. Woo, C.S. Lee, J.S. Park, H. Seo, J.-H. Kim, J.H. Song, Electrochemical investigation on high-rate properties of graphene nanoplatelet-carbon nanotube hybrids for Li-ion capacitors, J. Electroanal. Chem. 863 (2020), 114060.

[11] Y. Xue, Y. Li, G. Luo, K. Shi, E. Liu, J. Zhou, Using a dynamic inhibition concept to achieve content-controllable synthesis of N-coordinated Cu atoms as reversible active site toward super Li-ion capacitors, Adv. Energy Mater. 10 (2020) 2002644.

[12] C. Zhu, F. Wan, H. Ping, H. Wang, W. Wang, Z. Fu, Biotemplating synthesis of rodshaped tin sulfides assembled by interconnected nanosheets for energy storage, J. Power Sources 506 (2021), 230180.

[13] Q. Cheng, X. Yu, Structural engineering of metal-organic framework derived tin sulfides for advanced Li/Na storage, J. Mater. Chem. A 9 (2021) 11381-11396.

[14] X. Wu, H. Wu, B. Xie, R. Wang, J. Wang, D. Wang, Q. Shi, G. Diao, M. Chen, Atomic welded dual-wall hollow nanospheres for three-in-one hybrid storage mechanism of alkali metal ion batteries, ACS Nano (2021).

[15] B. Chen, D. Chao, E. Liu, M. Jaroniec, N. Zhao, S.-Z. Qiao, Transition metal dichalcogenides for alkali metal ion batteries: Engineering strategies at the atomic level, Energy Environ. Sci. 13 (2020) 1096-1131.

[16] B. Kurc, M. Pigfowska, L. Rymaniak, P. Fuc, Modern nanocomposites and hybrids as electrode materials used in energy carriers, Nanomaterials 11 (2021) 538.

[17] J. Wang, L. Sun, Y. Gong, L. Wu, C. Sun, X. Zhao, X. Shi, Y. Lin, K. Wang, Y. Zhang, A CNT/MoS_2@PPy composite with double electron channels and boosting charge transport for high-rate lithium storage, Appl. Surf. Sci. 566 (2021), 150693.

[18] R.A. Paredes Camacho A. Wu J. Liu L. Huang W. Yu H. Huang Sulfur-atom-expanded MoS2 nanosheets with enhanced lithium-ion storage Appl. Surf. Sci. 563 (2021) 150261.

[19] M. Naguib, M. Kurtoglu, V. Presser, J. Lu, J. Niu, M. Heon, L. Hultman, Y. Gogotsi, M.W. Barsoum, Two-dimensional nanocrystals produced by exfoliation of Ti3AlC2, Adv. Mater. 23 (2011) 4248-4253.

[20] X. Tang, X. Guo, W. Wu, G. Wang, 2D metal carbides and nitrides (MXenes) as high-performance electrode materials for lithium-based batteries, Adv. Energy Mater. 8 (2018) 1801897.

[21] Y. Zhu, K. Rajouá, S. Le Vot, O. Fontaine, P. Simon, F. Favier, Modifications of MXene layers for supercapacitors, Nano Energy 73 (2020), 104734.

[22] R. Zhang, Z. Xue, J. Qin, M. Sawangphruk, X. Zhang, R. Liu, NiCo-LDH/Ti3C2 MXene hybrid materials for lithium ion battery with high-rate capability and long cycle life, J. Energy Chem. 50 (2020) 143-153.

[23] W. Zhao, Y. Lei, Y. Zhu, Q. Wang, F. Zhang, X. Dong, H.N. Alshareef, Hierarchically structured $Ti_3C_2T_x$ MXene paper for Li-S batteries with high volumetric capacity, Nano Energy 86 (2021), 106120.

[24] Y. Zhou, K. Maleski, B. Anasori, J.O. Thostenson, Y. Pang, Y. Feng, K. Zeng, C. B. Parker, S. Zauscher, Y. Gogotsi, J.T. Glass, C. Cao, Ti3C2Tx MXene-reduced graphene oxide composite electrodes for stretchable supercapacitors, ACS Nano 14 (2020) 3576-3586.

[25] M. Zheng, R. Guo, Z. Liu, B. Wang, L. Meng, F. Li, T. Li, Y. Luo, MoS_2 intercalated p-Ti_3C_2 anode materials with sandwich-like three dimensional conductive networks for lithium-ion batteries, J. Alloys Compd. 735 (2018) 1262-1270.

[26] M. Chandran, A. Thomas, A. Raveendran, M. Vinoba, M. Bhagiyalakshmi, MoS_2 confined MXene heterostructures as electrode material for energy storage application, J. Energy Storage 30 (2020), 101446.

[27] X. Zhang, J. Li, L. Han, H. Li, J. Wang, T. Lu, L. Pan, In-situ fabrication of fewlayered MoS_2 wrapped on TiO_2-decorated MXene as anode material for durable lithium-ion storage, J. Colloid Interface Sci. 604 (2021) 30-38.

[28] K. Ma, H. Jiang, Y. Hu, C. Li, 2D nanospace confined synthesis of pseudocapacitance-dominated MoS_2-in-Ti_3C_2 superstructure for ultrafast and stable Li/Na-ion batteries, Adv. Funct. Mater. 28 (2018) 1804306.

[29] X. Wang, H. Li, H. Li, S. Lin, W. Ding, X. Zhu, Z. Sheng, H. Wang, X. Zhu, Y. Sun, 2D/2D 1T-MoS_2/Ti_3C_2 MXene heterostructure with excellent supercapacitor performance, Adv. Funct. Mater. 30 (2020) 0190302.

[30] L. Wang, X. Zhang, Y. Xu, C. Li, W. Liu, S. Yi, K. Wang, X. Sun, Z.-S. Wu, Y. Ma, Tetrabutylammonium-intercalated 1T-MoS_2 nanosheets with expanded interlayer spacing vertically coupled on 2D delaminated MXene for high-performance lithium-ion capacitors, Adv. Funct. Mater. 31 (2021) 2104286.

[31] D. Voiry, A. Mohite, M. Chhowalla, Phase engineering of transition metal dichalcogenides, Chem. Soc. Rev. 44 (2015) 2702-2712.

[32] Y. Cai, Y. Wang, L. Zhang, R. Fang, J. Wang, 3D heterostructure constructed by few-layered MXenes with a MoS_2 layer as the shielding shell for excellent hybrid capacitive deionization and enhanced structural stability, ACS Appl. Mater. Interfaces. 14 (2022) 2833-2847.

[33] J. Luo, W. Zhang, H. Yuan, C. Jin, L. Zhang, H. Huang, C. Liang, Y. Xia, J. Zhang, Y. Gan, X. Tao, Pillared structure design of MXene with ultralarge interlayer spacing for high-performance lithium-ion capacitors, ACS Nano 11 (2017) 2459-2469.

[34] O. Mashtalir, M.R. Lukatskaya, M.-Q. Zhao, M.W. Barsoum, Y. Gogotsi, Amine-assisted delamination of Nb2C MXene for Li-ion energy storage devices, Adv. Mater. 27 (2015) 3501-3506.

[35] E. Xu, Y. Zhang, H. Wang, Z. Zhu, J. Quan, Y. Chang, P. Li, D. Yu, Y. Jiang, Ultrafast kinetics net electrode assembled via MoSe2/MXene heterojunction for high-performance sodium-ion batteries, Chem. Eng. J. 385 (2020), 123839.

[36] C. Li, Z. Xue, J. Qin, M. Sawangphruk, P. Yu, X. Zhang, R. Liu, Synthesis of nickel hydroxide/delaminated-Ti_3C_2 MXene nanosheets as promising anode material for high performance lithium ion battery, J. Alloys Compd. 842 (2020), 155812.

[37] Y. Zhao, C. Liu, R. Yi, Z. Li, Y. Chen, Y. Li, I. Mitrovic, S. Taylor, P. Chalker, L. Yang, C. Zhao, Facile preparation of Co_3O_4 nanoparticles incorporating with highly conductive MXene nanosheets as high-performance anodes for lithium-ion batteries, Electrochim. Acta 345 (2020), 136203.

[38] S. Zhang, H. Ying, P. Huang, J. Wang, Z. Zhang, T. Yang, W.-Q. Han, Rational design of pillared SnS/$Ti_3C_2T_x$ MXene for superior lithium-ion storage, ACS Nano 14 (2020) 17665-17674.

[39] C. Shen, L. Wang, A. Zhou, H. Zhang, Z. Chen, Q. Hu, G. Qin, MoS_2-decorated Ti_3C_2 MXene nanosheet as anode material in lithium-ion batteries, J. Electrochem. Soc., 164 (2017) A2654-A2659.

[40] S. Luan, M. Han, Y. Xi, K. Wei, Y. Wang, J. Zhou, L. Hou, F. Gao, MoS2-decorated 2D Ti_3C_2 (MXene): A high-performance anode material for lithium-ion batteries, Ionics 26 (2020) 51-59.

[41] G. Du, M. Tao, W. Gao, Y. Zhang, R. Zhan, S. Bao, M. Xu, Preparation of MoS_2/ $Ti_3C_2T_x$ composite as anode material with enhanced sodium/lithium storage performance, Inorg. Chem. Front. 6 (2019) 117-125.

[42] Y. Dong, M. Yu, Z. Wang, Y. Liu, X. Wang, Z. Zhao, J. Qiu, A top-down strategy toward 3D Carbon nanosheet frameworks decorated with hollow nanostructures for superior lithium storage, Adv. Funct. Mater. 26 (2016) 7590-7598.

[43] J. Ai, Y. Lei, S. Yang, C. Lai, Q. Xu, SnS nanoparticles anchored on Ti_3C_2 nanosheets matrix via electrostatic attraction method as novel anode for lithium ion batteries, Chem. Eng. J. 357 (2019) 150-158.

[44] X. Liang, A. Garsuch, L.F. Nazar, Sulfur cathodes based on conductive MXene nanosheets for high-performance lithium-sulfur batteries, Angew. Chem. Int. Ed. 54 (2015) 3907-3911.

[45] J. Bai, B. Zhao, S. Lin, K. Li, J. Zhou, J. Dai, X. Zhu, Y. Sun, Construction of hierarchical V_4C_3-MXene/MoS_2/C nanohybrids for high rate lithium-ion batteries, Nanoscale 12 (2020) 1144-1154.

[46] Y. Liu, Y. He, E. Vargun, T. Plachy, P. Saha, Q. Cheng, 3D porous Ti3C2 MXene/ NiCo-MOF composites for enhanced lithium storage, Nanomaterials 10 (2020) 695.

[47] Z.-H. Zhao, X.-D. Hu, H. Wang, M.-Y. Ye, Z.-Y. Sang, H.-M. Ji, X.-L. Li, Y. Dai, Superelastic 3D few-layer MoS_2/carbon framework heterogeneous electrodes for highly reversible sodium-ion batteries, Nano Energy 48 (2018) 526-535.

[48] J. Ru, T. He, B. Chen, Y. Feng, L. Zu, Z. Wang, Q. Zhang, T. Hao, R. Meng, R. Che, C. Zhang, J. Yang, Covalent assembly of MoS_2 nanosheets with SnS nanodots as linkages for lithium/sodium-ion batteries, Angew. Chem. Int. Ed. 59 (2020) 14621-14627.

[49] Y. Cui, Z. Liu, Y. Zhang, P. Liu, M. Ahmad, Q. Zhang, B. Zhang, Wrinkled threedimensional porous MXene/Ni composite microspheres for efficient broadband microwave absorption, Carbon 181 (2021) 58-68.

[50] Z. Liu, H. Xiong, Y. Luo, L. Zhang, K. Hu, L. Zhang, Y. Gao, Z.-A. Qiao, Interface-induced self-assembly strategy toward 2D ordered mesoporous Carbon/MXene heterostructures for high-performance supercapacitors, ChemSusChem 14 (2021) 4422-4430.

[51] H. Zhang, P. Zhang, W. Zheng, W. Tian, J. Chen, Y. Zhang, Z. Sun, 3D d-Ti_3C_2 xerogel framework decorated with core-shell SnO2@C for high-performance lithium-ion batteries, Electrochim. Acta 285 (2018) 94-102.

[52] X. Yang, J. Mao, H. Niu, Q. Wang, K. Zhu, K. Ye, G. Wang, D. Cao, J. Yan, NiS_2/ MoS_2 mixed phases with abundant active edge sites induced by sulfidation and graphene introduction towards high-rate supercapacitors, Chem. Eng. J. 406 (2021), 126713.

[53] K.S.W. Sing, Reporting physisorption data for gas, solid systems with special reference to the determination of surface area and porosity (recommendations, Pure Appl. Chem. 57 (1985) (1984) 603-619.

[54] R. Dai, A. Zhang, Z. Pan, A.M. Al-Enizi, A.A. Elzatahry, L. Hu, G. Zheng, Epitaxial growth of lattice-mismatched core-shell TiO_2@MoS_2 for enhanced lithium-ion storage, Small 12 (2016) 2792-2799.

[55] Z. Sun, Y. Yao, J. Wang, X. Song, P. Zhang, L. Zhao, L. Gao, High rate lithium-ion batteries from hybrid hollow spheres with a few-layered MoS2-entrapped carbon sheath synthesized by a space-confined reaction, J. Mater. Chem. A 4 (2016) 10425-10434.

[56] Q. Li, J. Zhou, F. Li, Z. Sun, Novel MXene-based hierarchically porous composite as superior electrodes for Li-ion storage, Appl. Surf. Sci. 530 (2020), 147214.

[57] J. Pei, H. Geng, E.H. Ang, L. Zhang, X. Cao, J. Zheng, H. Gu, Controlled synthesis of hollow C@TiO_2@MoS_2 hierarchical nanospheres for high-performance lithium-ion batteries, Nanoscale 10 (2018) 17327-17334.

[58] Z. Hu, X. Kuai, J. Chen, P. Sun, Q. Zhang, H.-H. Wu, L. Zhang, Strongly coupled MoS_2 nanocrystal/Ti_3C_2 nanosheet hybrids enable high-capacity lithium-ion storage, ChemSusChem 13 (2020) 1485-1490.

[59] Y. Hao, S. Wang, Y. Shao, Y. Wu, S. Miao, High-energy density Li-ion capacitor with layered SnS_2/reduced graphene oxide anode and BCN nanosheet cathode, Adv. Energy Mater. 10 (2020) 1902836.

[60] G. Zou, Z. Zhang, J. Guo, B. Liu, Q. Zhang, C. Fernandez, Q. Peng, Synthesis of MXene/Ag composites for extraordinary long cycle lifetime lithium storage at high rates, ACS Appl. Mater. Interfaces. 8 (2016) 22280-22286.

[61] H. Tabassum, R. Zou, A. Mahmood, Z. Liang, Q. Wang, H. Zhang, S. Gao, C. Qu, W. Guo, S. Guo, A universal strategy for hollow metal oxide nanoparticles encapsulated into B/N Co-doped graphitic nanotubes as high-performance lithium-ion battery anodes, Adv. Mater. 30 (2018) 1705441.

[62] Y. Wang, W. Xie, D. Li, P. Han, L. Shi, Y. Luo, G. Cong, C. Li, J. Yu, C. Zhu, J. Xu, One-pot synthesis of hierarchical $Co_{1-x}S$/NC@MoS_2/C hollow nanofibers based on one-dimensional metal coordination polymers for enhanced lithium and sodium-ion storage, Sci. Bull. 65 (2020) 1460-1469.

[63] T. Brezesinski, J. Wang, S.H. Tolbert, B. Dunn, Ordered mesoporous a-MoO3 with iso-oriented nanocrystalline walls for thin-film pseudocapacitors, Nat. Mater. 9 (2010) 146-151.

[64] C. Wang, C. Zhan, X. Ren, R. Lv, W. Shen, F. Kang, Z.-H. Huang, MoS_2/carbon composites prepared by ball-milling and pyrolysis for the high-rate and stable anode of lithium ion capacitors, RSC Adv. 9 (2019) 42316-42323.

[65] H.-J. Zhang, Q.-C. Jia, L.-B. Kong, Multi-dimensional hybrid heterostructure MoS_2@C nanocomposite as a highly reversible anode for high-energy lithium-ion capacitors, Appl. Surf. Sci. 531 (2020), 147222.

[66] J. Ju, L. Zhang, H. Shi, Z. Li, W. Kang, B. Cheng, Three-dimensional porous carbon nanofiber loading MoS_2 nanoflake-flowerballs as a high-performance anode material for Li-ion capacitor, Appl. Surf. Sci. 484 (2019) 392-402.

[67] L. Yuan, X.-H. Lu, X. Xiao, T. Zhai, J. Dai, F. Zhang, B. Hu, X. Wang, L. Gong, J. Chen, C. Hu, Y. Tong, J. Zhou, Z.L. Wang, Flexible solid-state supercapacitors based on Carbon nanoparticles/MnO_2 nanorods hybrid structure, ACS Nano 6 (2012) 656-661.

[68] K. Krishnamoorthy, P. Pazhamalai, S. Sahoo, S.-J. Kim, Titanium carbide sheet based high performance wire type solid state supercapacitors, J. Mater. Chem. A 5 (2017) 5726-5736.

[69] P. Yu, G. Cao, S. Yi, X. Zhang, C. Li, X. Sun, K. Wang, Y. Ma, Binder-free 2D titanium carbide (MXene)/carbon nanotube composites for high-performance lithium-ion capacitors, Nanoscale 10 (2018) 5906-5913.

[70] H.-J. Zhang, Y.-K. Wang, L.-B. Kong, A facile strategy for the synthesis of threedimensional heterostructure self-assembled $MoSe_2$ nanosheets and their application as an anode for high-energy lithium-ion hybrid capacitors, Nanoscale 11 (2019) 7263-7276.

[71] Y. Wang, L. Maocheng, C. Jianyun, Z. Hujun, K. Lingbin, T.D. P., L. Xiaohong, W.F. C., 3D hierarchically structured CoS nanosheets: Li^+ storage mechanism and application of the high-performance lithium-ion capacitors, ACS Appl. Mater. Interfaces., 12 (2020) 3709-3718.

[72] A. Chaturvedi, P. Hu, V. Aravindan, C. Kloc, S. Madhavi, Unveiling twodimensional TiS_2 as an insertion host for the construction of high energy Li-ion capacitors, J. Mater. Chem. A 5 (2017) 9177-9181.

[73] Z. Chen, Z. Li, W. He, Y. An, L. Shen, H. Dou, X. Zhang, Nb_3O_7F mesocrystals: Orientation formation and application in lithium ion capacitors, CrystEngComm (2021).

[74] Z. Chen, H. Li, X. Lu, L. Wu, J. Jiang, S. Jiang, J. Wang, H. Dou, X. Zhang, Nitrogenated urchin-like Nb_2Os microspheres with extraordinary pseudocapacitive properties for lithium-ion capacitors, ChemElectroChem 5 (2018) 1516-1524.

[75] D. Yan, S.-H. Li, L.-P. Guo, X.-L. Dong, Z.-Y. Chen, W.-C. Li, Hard@soft integrated morning glory like porous Carbon as a cathode for a high-energy lithium ion capacitor, ACS Appl. Mater. Interfaces. 10 (2018) 43946-43952.